Supporting information

Effect of particle size on $LiNi_{0.6}Mn_{0.2}Co_{0.2}O_2$ layered oxide performance in Li-ion batteries

Adrien Soloy[1], Delphine Flahaut[2,5], Joachim Allouche[2,5], Dominique Foix[2,5], Germain Salvato Vallverdu[2,5], Emmanuelle Suard[3], Erwan Dumont[4], Lucille Gal[4], François Weill[1,5,6] and Laurence Croguennec[1,5,6,]*

[1] Univ. Bordeaux, CNRS, Bordeaux INP, ICMCB UMR 5026, F-33600 Pessac, France

[2] Université de Pau et des Pays de l'Adour, E2S UPPA, CNRS, IPREM UMR 5254, 64000 Pau, France

[3] Institut Laue-Langevin, 71 avenue des Martyrs, 38042 Grenoble, France

[4] SAFT, Direction de la Recherche, 33074 Bordeaux, France

[5] RS2E, Réseau Français sur le Stockage Electrochimique de l'Energie, FR CNRS 3459, F-80039 Amiens Cedex 1, France

[6] ALISTORE-ERI European Research Institute, FR CNRS 3104, F-80039 Amiens Cedex 1, France

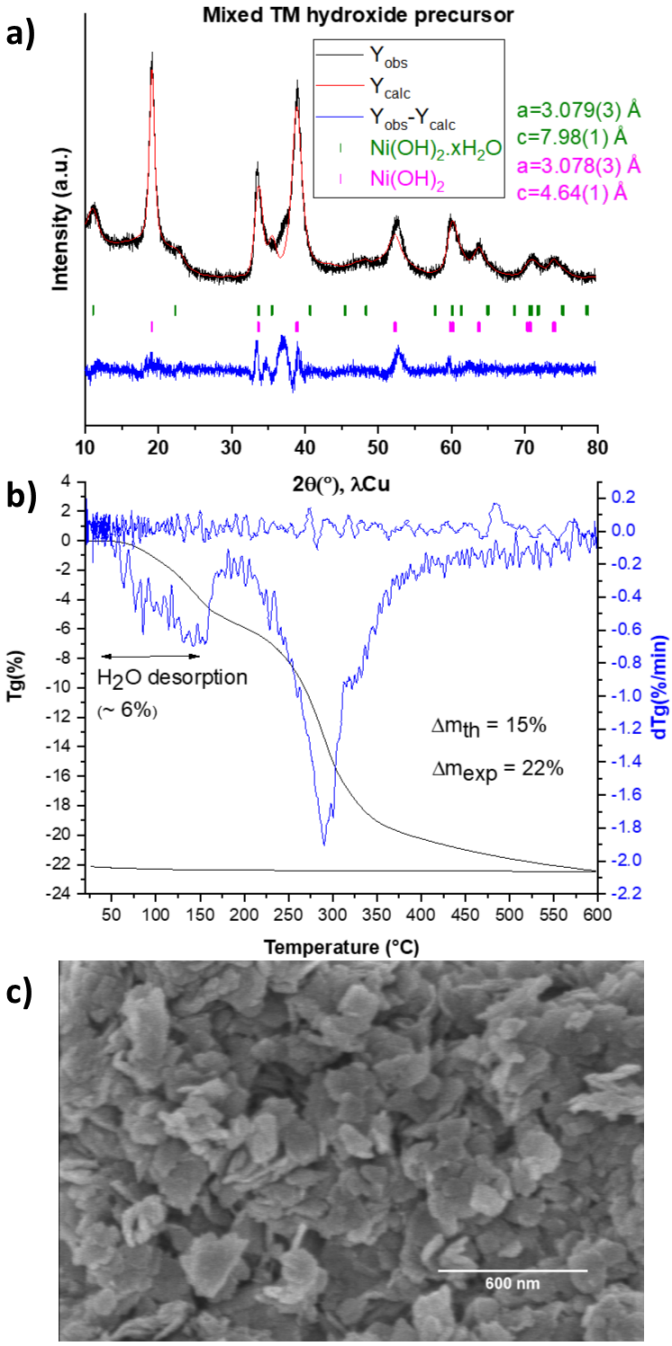

Figure S1. Mixed transition metal hydroxide precursor $Ni_{0.6}Mn_{0.2}Co_{0.2}(OH)_2$ characterization. a) XRD pattern and the corresponding Le Bail refinement. The obtained material is a mixture of $Ni(OH)_2$ type phases with a small amount of $Ni(OH)_2.xH_2O$. Both phases crystallize in the P-3m1 hexagonal space group. b) Thermogravimetric analysis. The experimental mass loss observed upon heating the hydroxide under air at 10°C/min is around 22 wt.% in total, with first

the desorption of H_2O between 50 and 175°C (ca. 6 wt.%) and then the formation of a mixture of transition metal oxides M_xO_y between 200°C and 600°C (ca. 16 wt.%). The experimental mass loss of 16 wt.% is in good agreement with the theoretical one calculated according to the chemical reaction $Ni_{0.6}Mn_{0.2}Co_{0.2}(OH)_2 + 0.13\ O_2 \rightarrow 0.6\ NiO + 0.2\ MnO_2 + 0.2/3\ Co_3O_4 + H_2O$ (i.e. 15 wt.%). c) Morphology of the hydroxide observed by SEM. The precursor particles are small platelets of 170 nm of length and 27 nm of thickness in average.

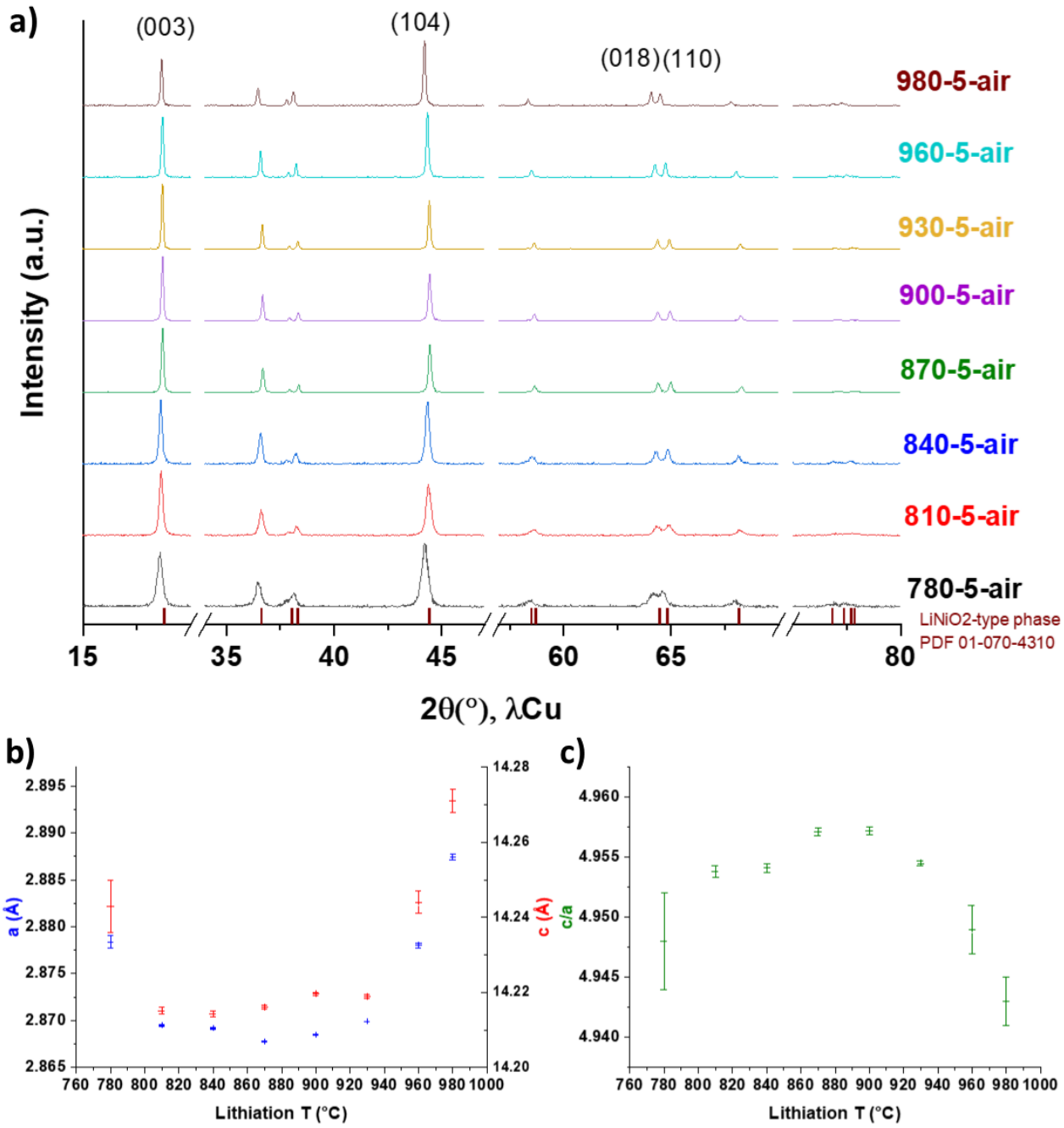

Figure S2. a) XRD patterns obtained after lithiations carried out in the temperature range 780-980°C. The samples are named according to the synthesis conditions used for their preparation: Lithiation temperature (°C) - weight percentage of Li_2CO_3 excess - atmosphere. For instance, 930-5-air is the name of the NMC 622 sample obtained after a thermal treatment at 930°C, with a 5 wt.% excess of Li_2CO_3, and under air. b-c) Evolution of lattice parameters and c/a ratios

depending on the synthesis temperature. They were determined by Rietveld refinement of those patterns. In the temperature range of 810-930°C the materials show structures closer to the ideal 2D layered structure, with the smaller lattice parameters and the higher c/a ratios. Differences in the standard deviations are observed in b) and c) due to the fact that 35h diffraction analyses were performed for the samples synthesized between 810°C and 930°C while only 35 min analyses were done for the others.

Table S1. Chemical analyses of the synthesized samples performed by ICP-OES.

	ICP-OES analyses			
Samples	**Ni/ΣTM**	**Mn/ΣTM**	**Co/ΣTM**	**Li/ΣTM**
930-5-O_2	0.60(3)	0.20(1)	0.20(1)	1.07(8)
930-5-air	0.62(4)	0.19(1)	0.19(1)	1.00(7)
900-5-O_2	0.60(3)	0.20(1)	0.20(1)	1.06(7)
900-1-air	0.58(5)	0.21(2)	0.21(1)	1.06(7)
900-5-air	0.6(1)	0.20(2)	0.20(2)	1.1(1)
870-1-air	0.60(5)	0.20(1)	0.21(1)	1.04(7)
870-5-air	0.62(6)	0.19(2)	0.19(1)	1.1(1)
840-1-air	0.58(6)	0.21(2)	0.21(1)	1.02(8)
840-5-air	0.62(6)	0.19(2)	0.19(1)	1.08(9)
810-5-O_2	0.60(3)	0.20(1)	0.20(1)	1.06(7)
810-5-air	0.62(5)	0.19(2)	0.19(1)	1.03(8)

Table S2. Structural parameters determined for the 810-5-air sample by the Rietveld refinement of its Neutron (upper line) and X-ray diffraction (lower line, in italics) patterns. On the contrary to neutron diffraction, it is not possible to distinguish Ni, Mn and Co by X-ray diffraction.

810-5-air sample Space group: *R-3m*, *Z*=3 *a = 2.86952(9) Å = b; c = 14.2152(9) Å; c/a = 4.9539(5)* Neutron diffraction*:* R_{wp} = 4.09%; R_p = 3.23%; R_{bragg} = 6.50% *XRD:* R_{wp} *= 2.46%;* R_p *= 1.93%;* R_{bragg} *= 4.33%*						
Atom	**Wyckoff position**	**x/a**	**y/b**	**z/c**	**Biso**	**Occ.**
Li	3b	0	0	½	1.0(4) *1.0(0)*	0.961(3) *0.965(0)*
Ni	3b	0	0	½	1.0(4) *1.0(0)*	0.039(3) *0.035(0)*
Ni	3a	0	0	0	0.7(1) *0.43(5)*	0.573(3) *1.000(0)*
Mn	3a	0	0	0	0.7(1) */*	0.214(0) */*
Co	3a	0	0	0	0.7(1) */*	0.214(0) */*
O	6c	0	0	0.2584(3) *0.2591(2)*	0.94(7) *0.23(9)*	1 *1*

Table S3. BET surface areas and pore volumes determined for the 3 samples.

Sample	Average primary particle size	BET surface area (m^2/g)	Pore volume (cm^3/g)
930-5-O_2	2.1 μm	1	0.002
900-5-O_2	810 nm	2	0.003
810-5-O_2	240 nm	3	0.009

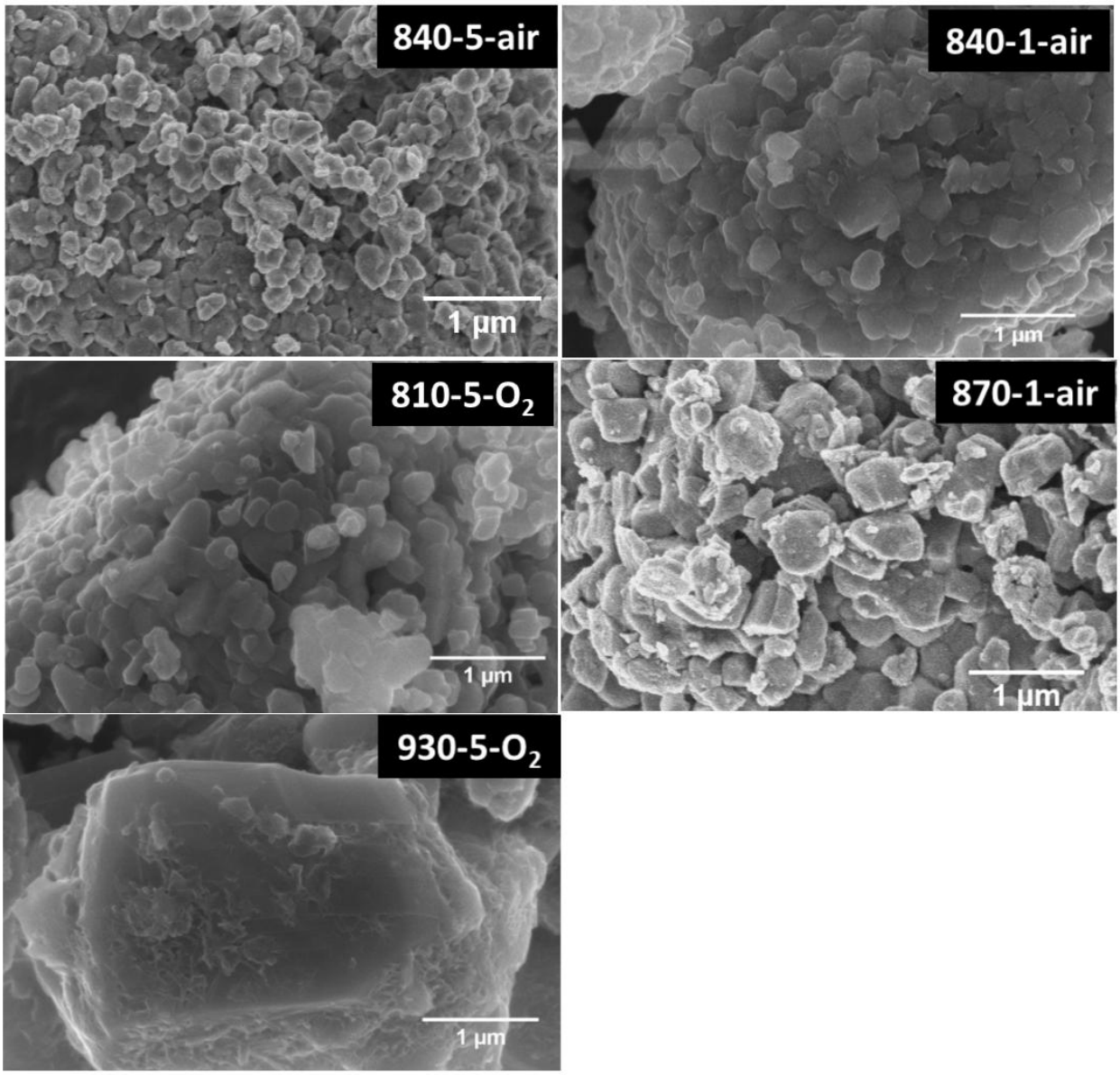

Figure S3. Morphologies of the 5 other samples that are part of the 11 selected samples.

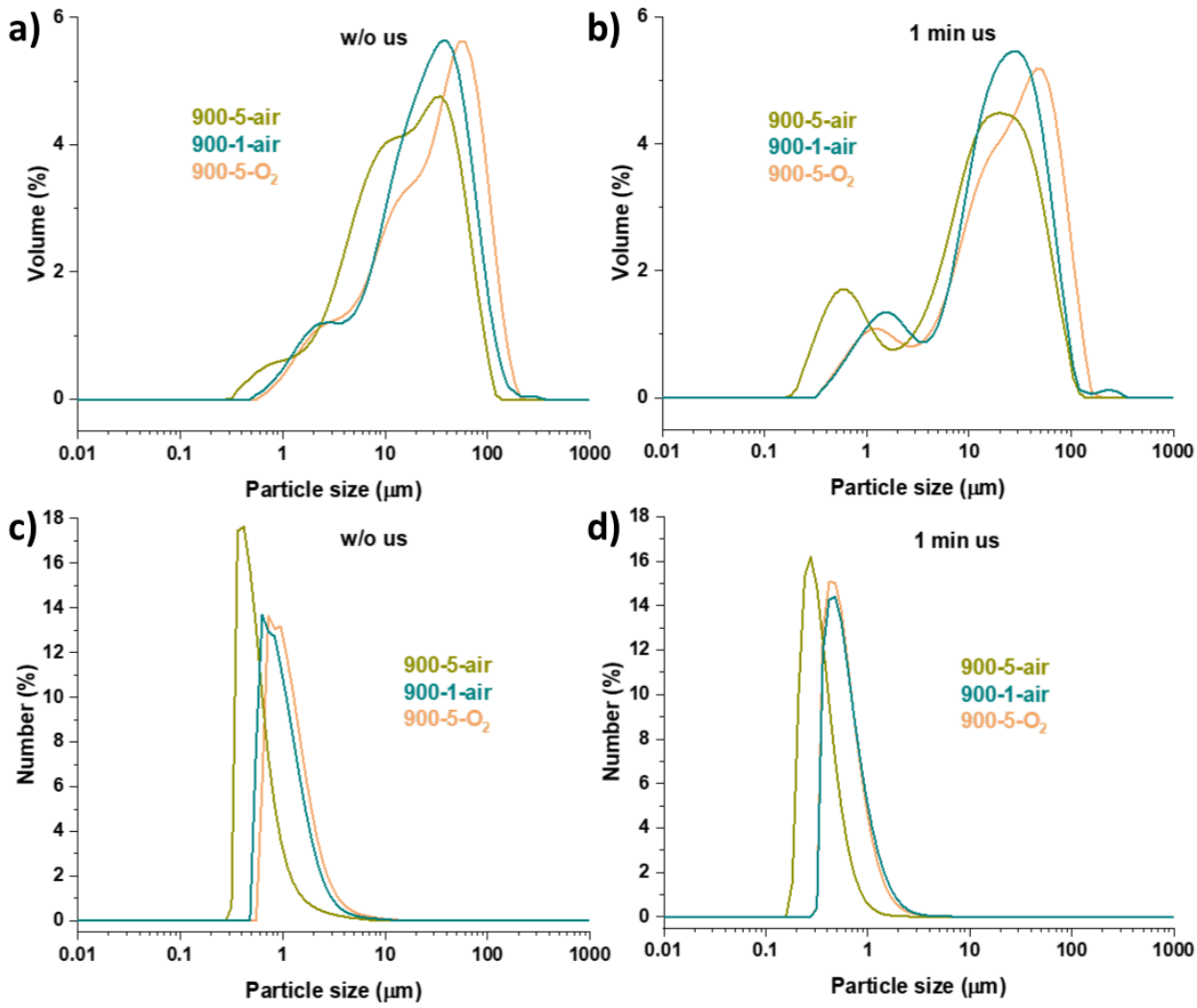

Figure S4. Secondary particle size distribution for the samples synthesized at 900°C. Size distribution in volume percentage without sonication (a) and with 1 min sonication (b), as well as in number in percentage without sonication (c) and with 1 min sonication (d).

Table S4. XPS quantitative analyses of the 900-5-air sample (400 nm particles).

Peak	Assignment	BE (eV)	At %
C 1s	**C-C/C-H**	285.0	17.2
	C-O	286.4	1.3
	C=O/O-C=O	288.6	1.1
	CO_3	290.1	10.0
Li 1s	**NMC**	54.4	2.2
	Li_2CO_3	55.6	30.4
O 1s	**NMC**	529.7	1.6
	Surface	531.9	31.8
	Surface	534.0	0.9
Ni 3p	**Ni**	68.1	1.6
Co 3p	**Co**	61.3	0.4
Mn 3p	**Mn**	50.0	0.4
S $2p_{3/2-1/2}$	**S**	170.0	1.2

Table S5. Transition metal ratios obtained for all materials from Ni, Mn and Co atomic percentages extracted from the global quantitative analyses performed from XPS spectra.

		Atomic percentages				
Samples	**Average particle size**	**Ni 3p**	**Mn 3p**	**Co 3p**	**ΣTM**	**(Ni:Mn:Co)/ΣTM**
930-5-O_2	2.1 µm	4.1	1.0	1.0	6.1	0.67 : 0.16 : 0.16
930-5-air	1.2 µm	1.8	0.5	0.5	2.8	0.64 : 0.18 : 0.18
900-5-O_2	810 nm	5.8	1.3	1.4	8.5	0.68 : 0.15 : 0.16
900-1-air	1.1 µm	4.9	1.1	1.2	7.2	0.68 : 0.15 : 0.17
900-5-air	400 nm	1.6	0.4	0.4	2.4	0.67 : 0.17 : 0.17
870-1-air	370 nm	4.9	1.4	1.2	7.5	0.65 : 0.19 : 0.16
870-5-air	280 nm	1.6	0.7	0.4	2.7	0.59 : 0.26 : 0.15
840-1-air	240 nm	6.0	1.8	1.1	8.9	0.67 : 0.20 : 0.12
840-5-air	200 nm	3.5	1.9	0.9	6.3	0.56 : 0.30 : 0.14
810-5-O_2	240 nm	5.8	1.5	1.5	8.8	0.66 : 0.17 : 0.17
810-5-air	170 nm	1.7	1.0	0.6	3.3	0.52 : 0.30 : 0.18

Table S6. Comparison of the contribution of the carbonates species in the C 1s and Li 1s spectra, and the contribution of oxygen from the electrode material in atomic percentages extracted from the global quantitative analyses performed from XPS spectra of all materials.

		Atomic percentages		
Samples	**Average particle size**	**C 1s (Li_2CO_3)**	**Li 1s (Li_2CO_3)**	**% O_{NMC} in O1s**
930-5-O_2	2.1 µm	9.1	18.8	14.8
930-5-air	1.2 µm	11.3	22.6	6.0
900-5-O_2	810 nm	6.3	12.7	23.5
900-1-air	1.1 µm	6.2	13.6	22.4
900-5-air	400 nm	10.0	30.4	4.7
870-1-air	370 nm	6.0	12.1	23.6
870-5-air	280 nm	11.1	23.0	7.5
840-1-air	240 nm	5.4	11.1	27.0
840-5-air	200 nm	9.0	17.1	20.6
810-5-O_2	240 nm	6.2	13.0	27.0
810-5-air	170 nm	8.2	16.6	13.4

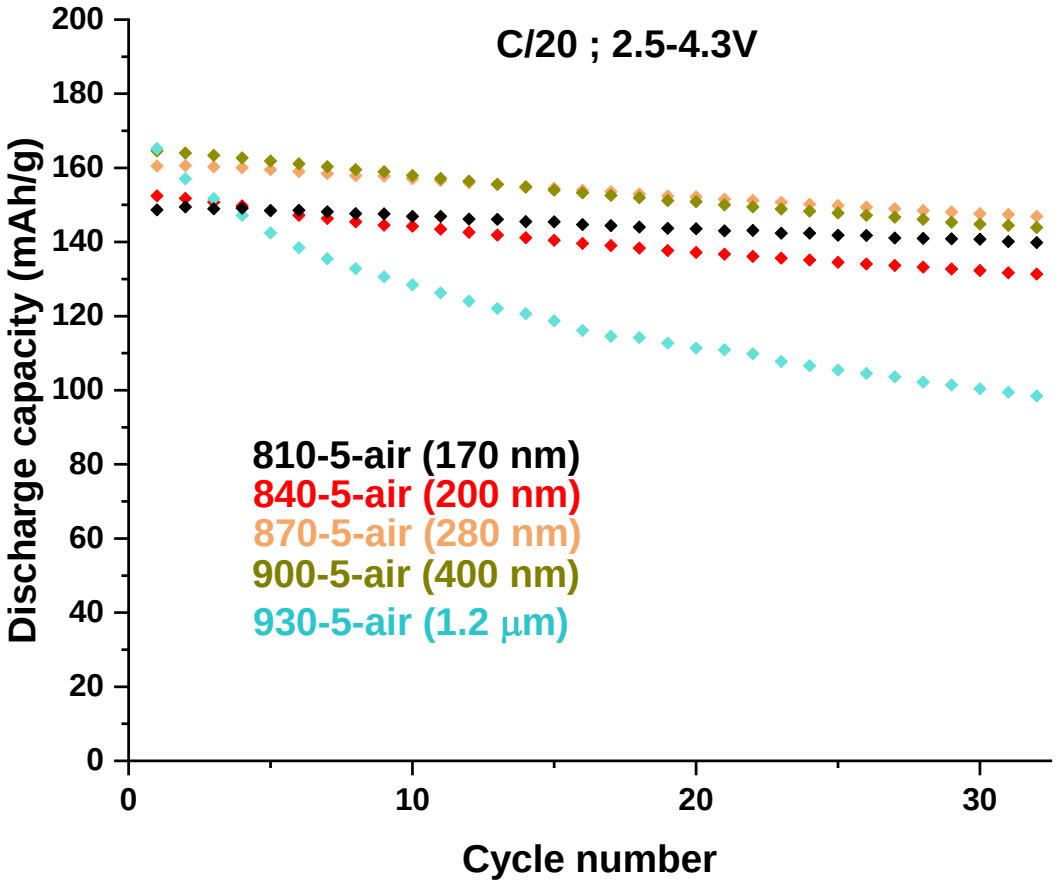

Figure S5. Discharge capacities as a function of the cycle number for the "5-air" samples cycled at C/20 in the 2.5-4.3V potential range.

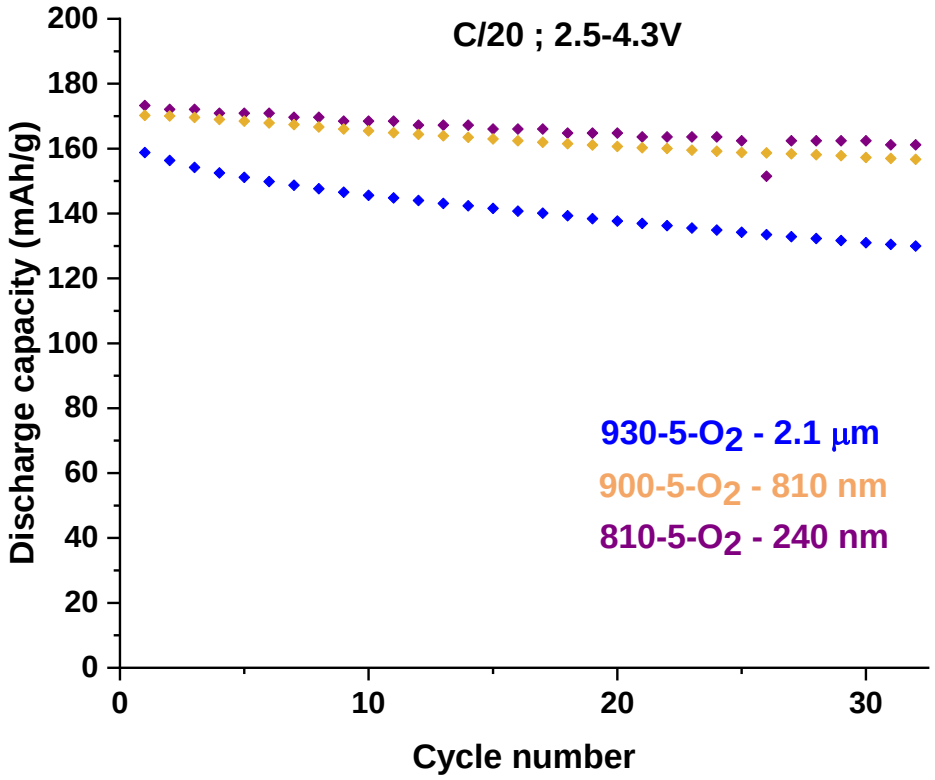

Figure S6. Discharge capacities as a function of the cycle number for the "5-O_2" samples cycled at C/20 in the 2.5-4.3V potential range.

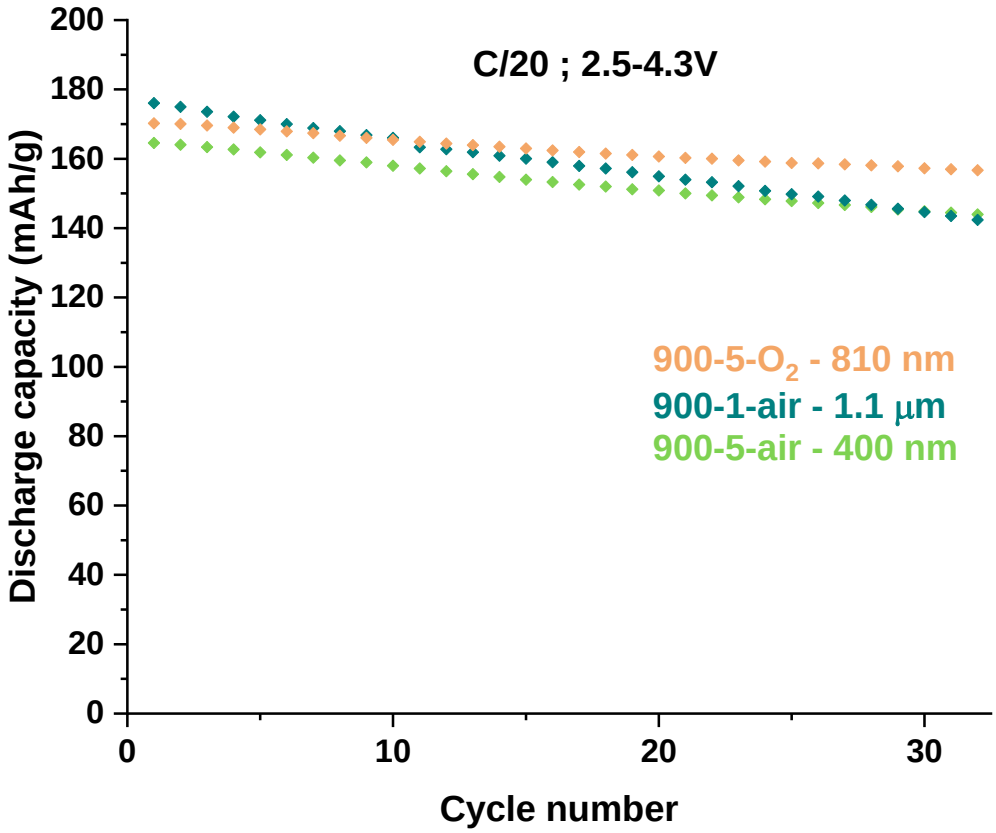

Figure S7. Discharge capacities as a function of the cycle number for the samples synthesized at 900°C cycled at C/20 in the 2.5-4.3V potential range.

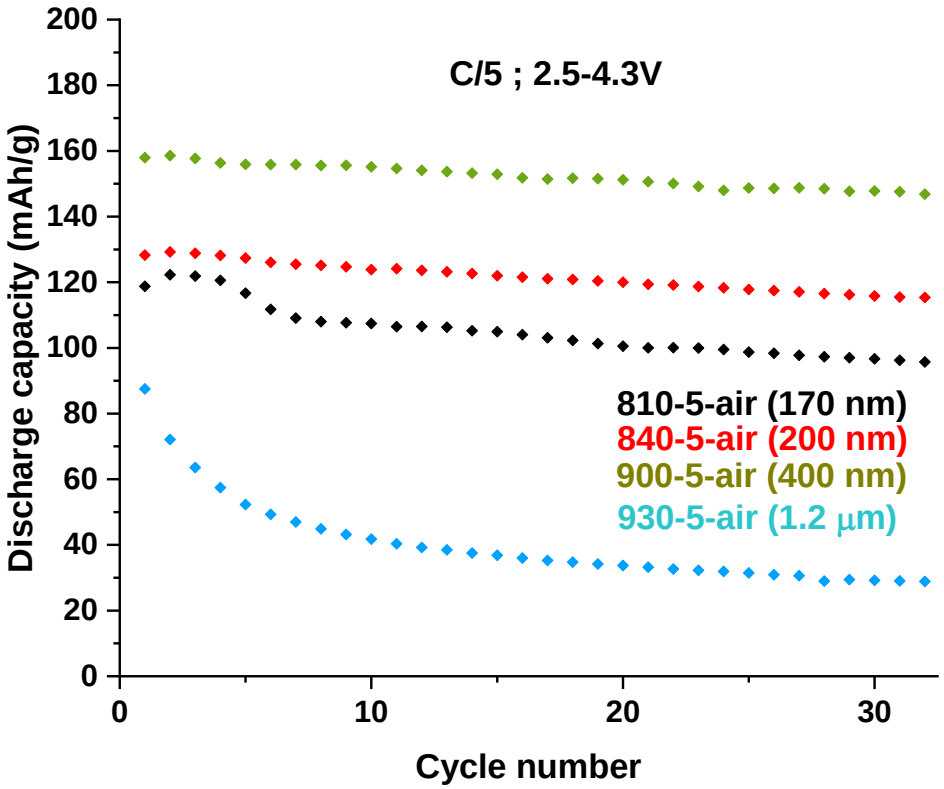

Figure S8. Discharge capacities as a function of the cycle number for 4 samples representative of the "5-air" series, cycled at C/5 in the potential range of 2.5-4.3V.

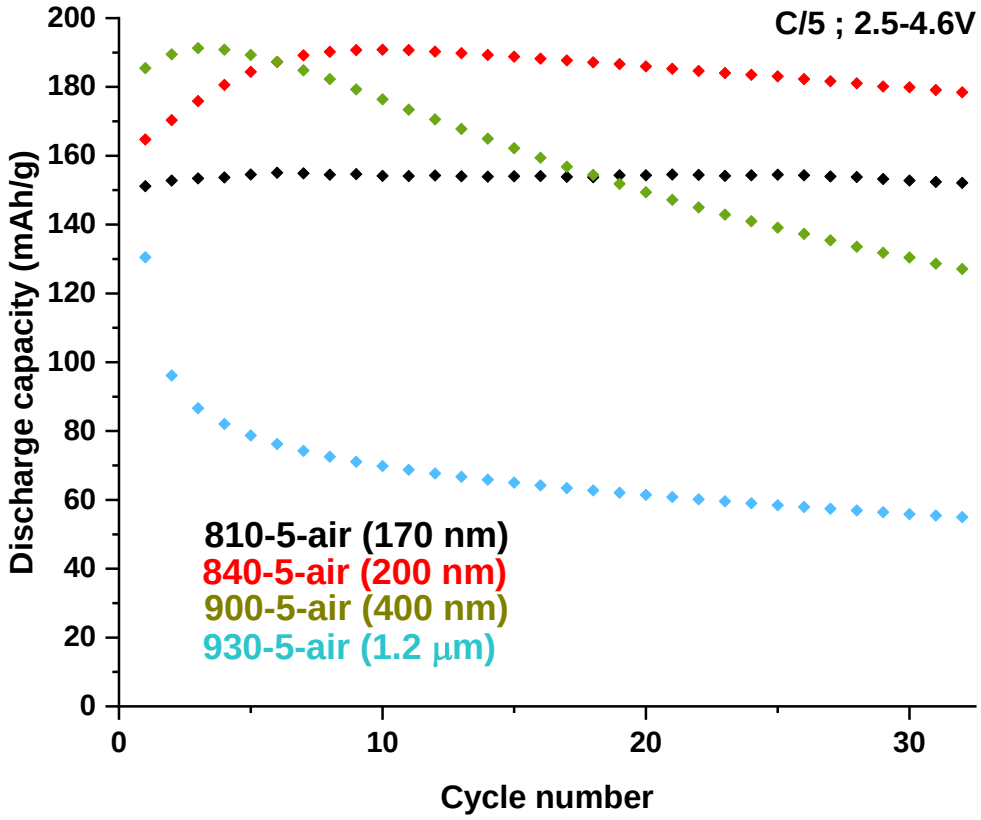

Figure S9. Discharge capacities as a function of the cycle number for 4 samples representative of the "5-air" series, cycled at C/5 in the potential range of 2.5-4.6V.

As explained by Wang et al., cycling to higher cut off voltage can generate microcracks at the surface of the particles and also the formation of a small amount of cubic phase due to the highly oxidative environment, making the contact between the SEI and the particles less good and creating pathways for Li ions.[59] The lower stability of the SEI and the lower amount of resistive LiF at the surface of the electrodes would reduce the charge transfer resistance at the interface and would explain the increasing capacities observed for the first cycles (or activation cycles as mentioned earlier) for the 200 nm and 400 nm particles (840-5-air and 900-5-air sample respectively) (Figure S9). It can be inferred that, after some cycles, the volume changes become less important and the SEI becomes more stable. The degradation products would then settle

more easily at the surface of the electrode, this would increase the charge transfer resistance at the interface and make the capacities decrease gradually, as observed in Figure S9. The fact that the capacities start decreasing after a less important number of cycles and decrease faster for the 400 nm particles (900-5-air) compared to the 200 nm particles (840-5-air) can be explained by the more important amount of Li_2CO_3 at the surface of the 400 nm particles (900-5-air), as shown in Table S5.

Table S7. XPS quantitative analyses of the 900-5-air electrode (400 nm particles) cycled at C/20 in the 2.5-4.3V potential range.

Peak	Attribution	BE (eV)	At %
C 1s	**C-C/C-H**	285.1	10.2
	C-O	286.3	4.2
	C=O	287.5	3.9
	CO_2	288.8	2.8
	CO_3	290.1	1.5
	CH_2 (PVDF)	286.5	3.9
	CF_2 (PVDF)	291.0	3.9
	CB	284.5	11.6
F 1s	**LiF**	685.1	9.5
	$Li_xPF_yO_z$	686.1	1.1
	CF_2 (PVDF)	688.0	7.9
	CF_3 (PVDF)	689.6	0.2
Li 1s	**NMC**	54.3	1.9
	Li_2CO_3	55.5	2.8
	$LiF/Li_xPF_yO_z$	56.1	19.4
O 1s	**NMC**	529.6	0.5
	CO_3, CO_2, O=C	531.9	3.5
	O-C	533.0	5.2
	O-P	534.2	3.4
Ni 3p	**Ni**	68.1	0.4
Mn 3p	**Mn**	50.0	0.3
Co 3p	**Co**	61.3	0.1
N 1s	**N**	400.4	0.2
P $2p_{3/2-1/2}$	**$Li_xPF_yO_z$**	135.0	1.5
S $2p_{3/2-1/2}$	**S**	165.0	0.3

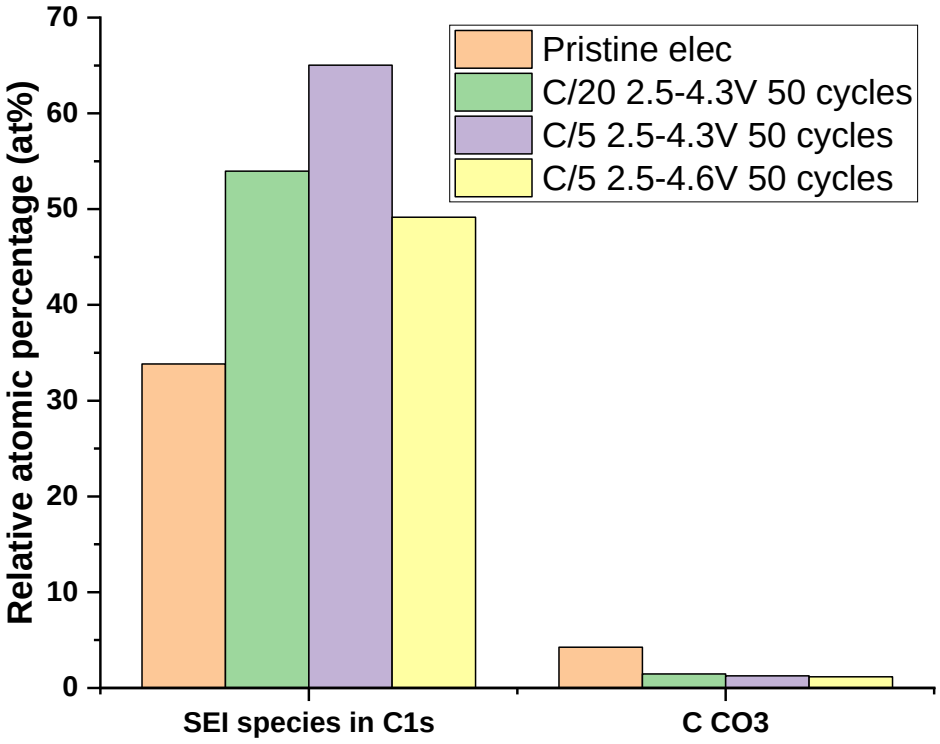

Figure S10. Evolution of atomic percentage (at.%) of carbonaceous species due to the solvents degradation in the C1s spectra (% SEI species in C1s) and of the C_{CO_3} contribution (% C CO_3) at the surface of 900-5-air pristine and cycled electrodes.

Table S8. Comparison of the contributions in atomic percentages of carbon black (CB), PVDF, active material, $LiF/Li_xPF_yO_z$ species and carbonaceous species extracted from the global quantitative analyses performed from XPS spectra of the 900-5-air electrodes cycled in different conditions. They are compared to the contributions obtained for the 900-5-air pristine electrode.

	Pristine electrode	**C/20 ; 2.5-4.3V ; 50 cycles**	**C/5 ; 2.5-4.3V ; 50 cycles**	**C/5 ; 2.5-4.6V ; 50 cycles**
Carbon black (CB)	25.1	11.6	6.1	8.4
PVdF	26.0	15.8	11.0	21.5
Active material (AM)	2.6	3.2	4.4	3.4
$LiF/Li_xPF_yO_z$	2.7	34.9	46.2	37.6
Carbonaceous species	43.7	34.1	32.0	28.9
SEI species in C1s	33.8	54.0	65.0	49.2
C_{CO_3}	4.3	1.5	1.3	1.2

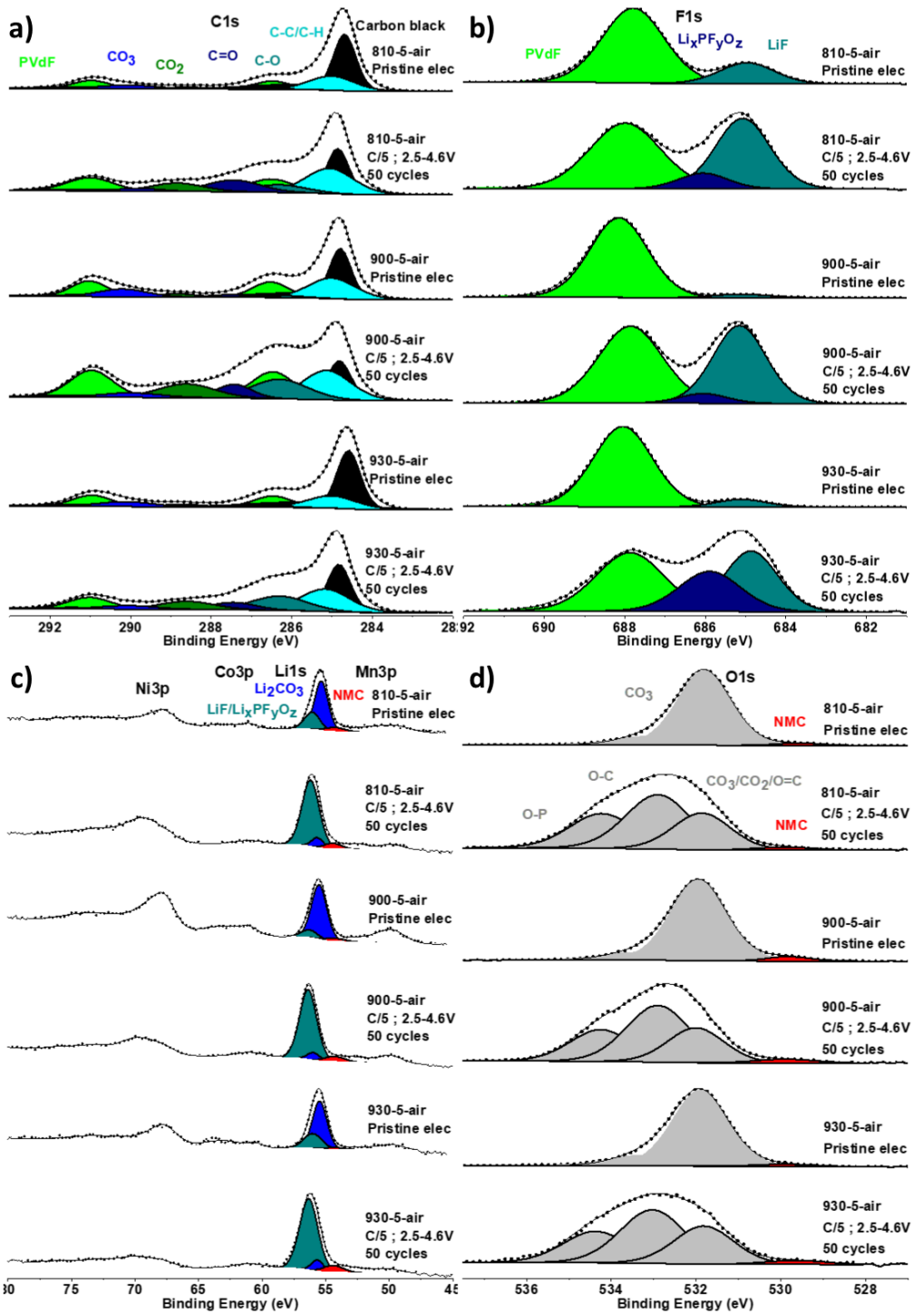

Figure S11. C1s (a), F1s (b) Li1s, Ni3p, Co3p, Mn3p (c) and O1s (d) XPS spectra of the 810-5-air, 900-5-air and 930-5-air pristine electrodes and of the same electrodes cycled for 50 cycles at C/5 between 2.5 and 4.6V. The dots and the lines represent the experimental and the fitted data respectively.

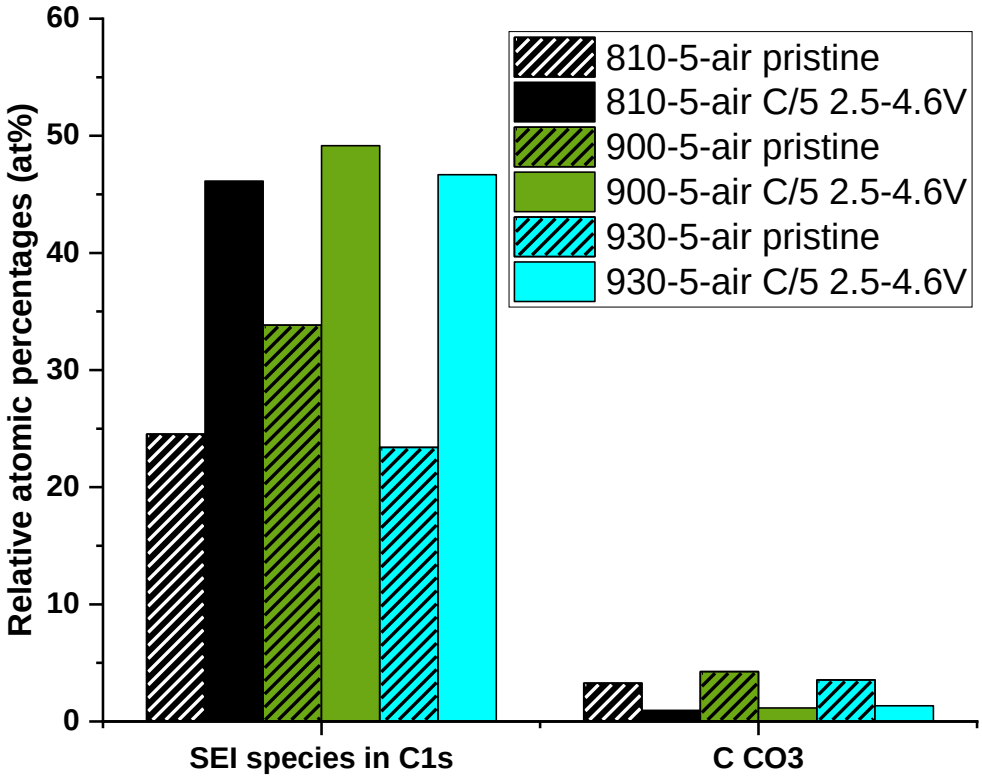

Figure S12: Evolution of atomic percentage (at.%) of carbonaceous species due to the solvents degradation in the C1s spectra (% SEI species in C1s) and of the C_{CO_3} contribution (% C CO_3) at the surface of 810-5-air, 900-5-air and 930-5-air electrodes cycled at C/5 in the 2.5-4.6 potential range and their corresponding pristine electrodes.

Table S9. Comparison of the contributions in atomic percentages of carbon black (CB), PVdF, active material, LiF/LixPFyOz species and carbonaceous species extracted from the global quantitative analyses performed from XPS spectra of the 810-5-air, 900-5-air and 930-5-air electrodes cycled at C/5; 2.5-4.6V. They are compared to the contributions obtained for the corresponding pristine electrodes.

	810-5-air Pristine electrode	**810-5-air C/5 ; 2.5-4.6V ; 50 cycles**	**900-5-air Pristine electrode**	**900-5-air C/5 ; 2.5-4.6V ; 50 cycles**	**930-5-air Pristine electrode**	**930-5-air C/5 ; 2.5-4.6V ; 50 cycles**
Carbon black (CB)	41.1	15.7	25.1	8.4	36.8	15.5
PVdF	18.9	17.9	26.0	21.5	24.3	15.6
Active material (AM)	1.7	2.7	2.6	3.4	1.4	3.2
$LiF/Li_xPF_yO_z$	5.4	30.4	2.7	37.6	4.5	36.7
Carbonaceous species	32.9	32.7	43.7	28.9	33.1	28.6
SEI species in C1s	24.5	46.1	33.8	49.2	23.4	46.7
C_{CO_3}	3.3	1.0	4.3	1.2	3.5	1.3

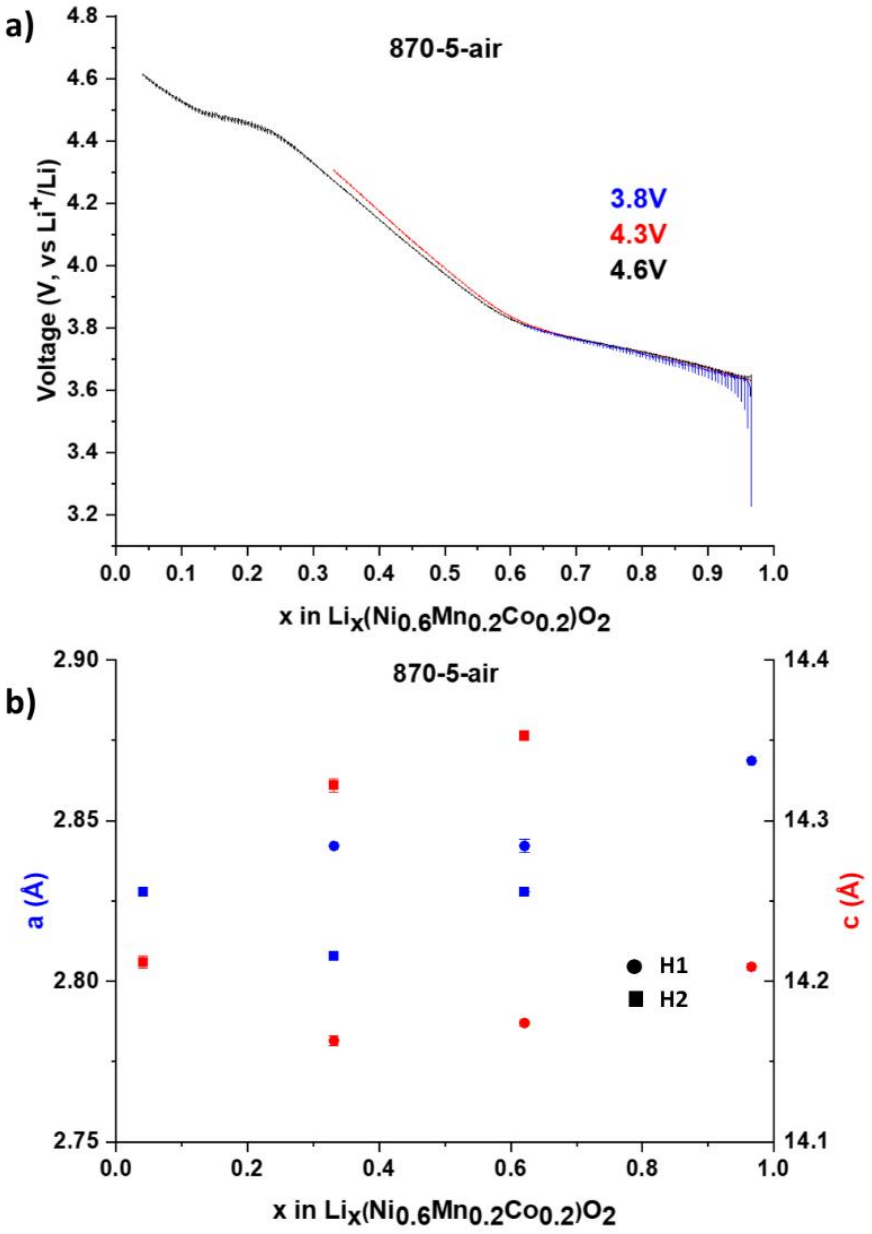

Figure S13. a) GITT curves stopped at 3.8V (blue), 4.3V (red) and 4.6V (black) during the 1st charge; b) lattice parameters determined from Rietveld refinements of *ex situ* XRD patterns collected for 870-5-air GITT electrodes.

GITT experiments were performed with the 280 nm particles to estimate the volume changes observed upon cycling of these NMC 622 samples. Different coin cells were cycled and stopped

at different stages of the 1st charge: 3.8, 4.3 and 4.6V (Figure S13a). This sample was chosen because it corresponds to medium-sized particles among all the materials of the "5-air" series and it is one of the samples giving the best electrochemical performances. After dismantling the coin cells, the electrodes were recovered and analysed by *ex situ* XRD, the changes in lattice parameters were determined by Le Bail refinement of the corresponding XRD patterns (Figure S13b). When Li^+ ions are deintercalated from the structure, the $c_{hex.}$ parameter increases at the beginning of charge before decreasing at the end of charge, while the $a_{hex.}$ parameter decreases continuously.[60–62] Those variations lead to the coexistence of 2 phases described in the $R\bar{3}m$ space group: H1 and H2.[63,64] Figure S13b shows the variations of the $a_{hex.}$ and $c_{hex.}$ parameters obtained at each state of charge for the H1 and H2 phases. These results show that charging up to 4.6V (and reaching a lithiation ratio of 0.1) causes, as expected, an increase followed by a decrease of the c_{hex} parameter, and thus more volume changes ("breathing"). On the contrary, charging up to a limited potential of 4.3V (and reaching a lithiation ratio of 0.3) prevents this decrease observed at high state of charge and thus minimizes volume changes. Indeed, when charging up to 4.3V, the H1→H2 phase transition leads to an increase of 1.1% of the c_{hex} parameter (from 14.163(3) Å to 14.322(3) Å), as well as a decrease of 1.2% of the a_{hex} parameter (from 2.842(2) Å to 2.8077(5) Å) at 4.3V inducing a global lattice volume decrease of 1.3%. When charging further up to 4.6V, higher state of charge is reached and the c_{hex} parameter of the H2 phase undergoes a slight decrease of 0.8% (from 14.322(3) Å to 14.212(4) Å) and the a_{hex} parameter undergoes a slight increase of 0.7% (from 2.8077(5) Å to 2.8277(5) Å) leading to a global lattice volume increase of 0.6% between 4.3 and 4.6V. When cycling at C/5, the lithiation ratio reached at 4.6V by the 400 nm particles is of 0.2 (vs. 0.1 for the 280 nm particles in GITT conditions) while it is of 0.35 (vs. 0.3 for the 280 nm particles in GITT conditions) at 4.3V, we

can thus assume the lattice parameters of the 400 nm particles change in a similar way than for the 280 nm particles when cycling at those potentials. Changes in lattice parameters upon cycling can lead to strains at the primary particle level. Depending on their amount and nature, cracks can be formed to accommodate these strains, with generation of new fresh surfaces in contact with the electrolyte. Larger primary particles are expected to be more prone to the formation of intragranular cracks and thus to intergranular decohesion within the aggregates (for instance, as discussed in the main text for 400 nm particles versus the 200 nm ones).

AUTHOR INFORMATION

Corresponding author

* Laurence Croguennec

Laurence.Croguennec@icmcb.cnrs.fr